

1
2
3
4
5

6
7
8
9
10
11
12
13
14
15
16
17
18
19
20

21
22
23

24

25
26
27
28

Supplementary information for:

Negative durotaxis: cell movement toward softer environments

Aleksi Isomursu^{1,†}, Keun-Young Park^{2,†}, Jay Hou^{3,†}, Bo Cheng^{4,5,†}, Mathilde Mathieu¹, Ghaidan Shamsan³, Benjamin Fuller³, Jesse Kasim³, M. Mohsen Mahmoodi², Tian Jian Lu^{6,7}, Guy M. Genin^{4,5,8}, Feng Xu^{4,5}, Min Lin^{4,5,*}, Mark Distefano^{2,*}, Johanna Ivaska^{1,9,10,*}, and David J. Odde^{3,*}

¹Turku Bioscience Centre, University of Turku and Åbo Akademi University, 20520 Turku, Finland

²Department of Chemistry, University of Minnesota, Minneapolis 55455, MN, USA

³Department of Biomedical Engineering, University of Minnesota, Minneapolis 55455, MN, USA

⁴The Key Laboratory of Biomedical Information Engineering of Ministry of Education, School of Life Science and Technology, Xi'an Jiaotong University, Xi'an 710049, P.R. China

⁵Bioinspired Engineering and Biomechanics Center (BEBC), Xi'an Jiaotong University, Xi'an 710049, P.R. China

⁶State Key Laboratory of Mechanics and Control of Mechanical Structures, Nanjing University of Aeronautics and Astronautics, Nanjing 210016, P.R. China

⁷MOE Key Laboratory of Multifunctional Materials and Structures, Xi'an Jiaotong University, Xi'an 710049, P.R. China

⁸NSF Science and Technology Center for Engineering Mechanobiology, Washington University in St. Louis, St. Louis 63130, MO, USA

⁹Department of Life Technologies, University of Turku, 20520 Turku, Finland

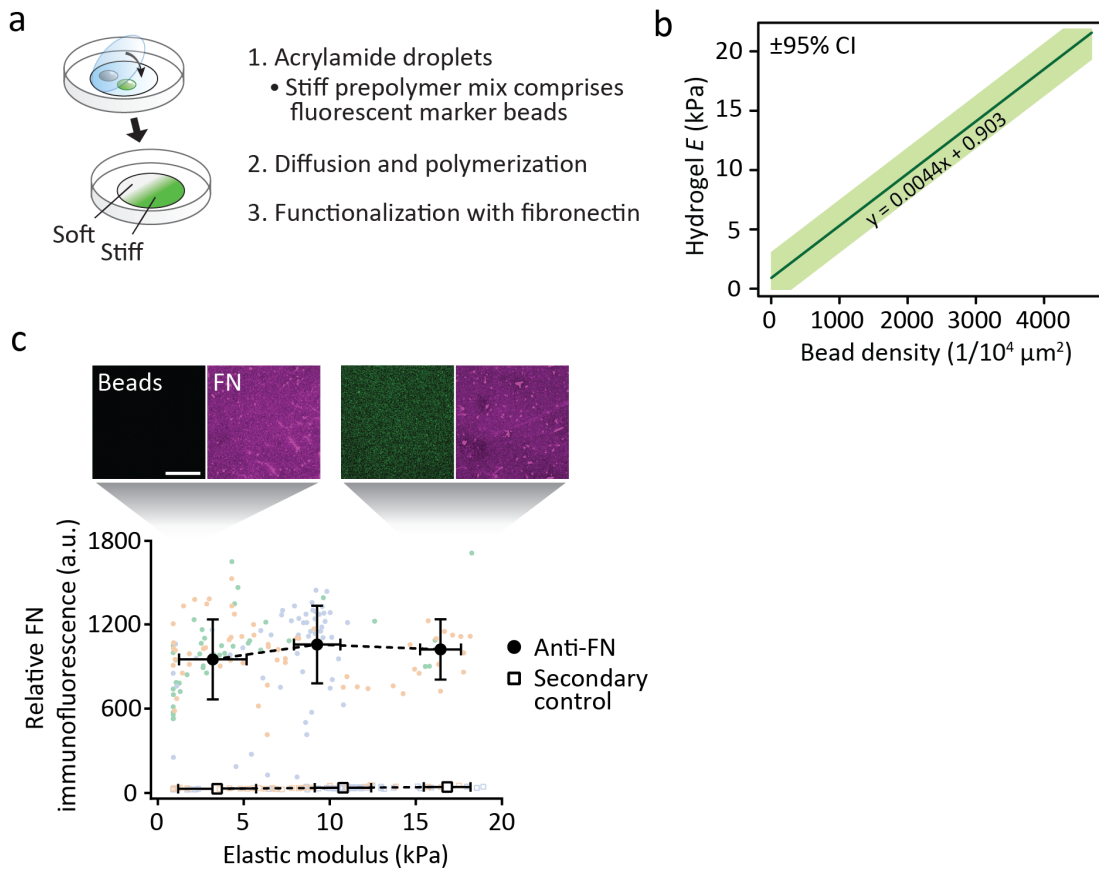
¹⁰InFlames Research Flagship Center, University of Turku, 20520 Turku, Finland

[†]These authors have contributed equally to the work

*Correspondence to: oddex002@umn.edu (D.J.O.); johanna.ivaska@utu.fi (J.I.); diste001@umn.edu (M.D.); minlin@xjtu.edu.cn (M.L.)

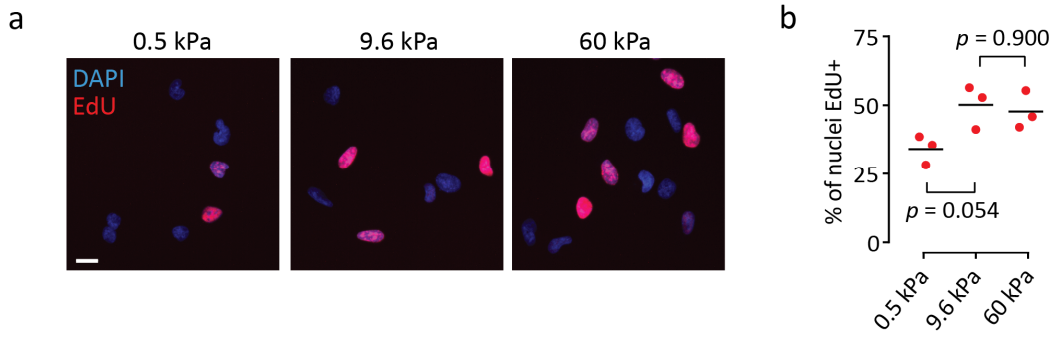
This file includes:

- Figures S1–S15
- Supplementary Texts 1–3
- Tables S1–S3
- Captions for Movies S1–S3



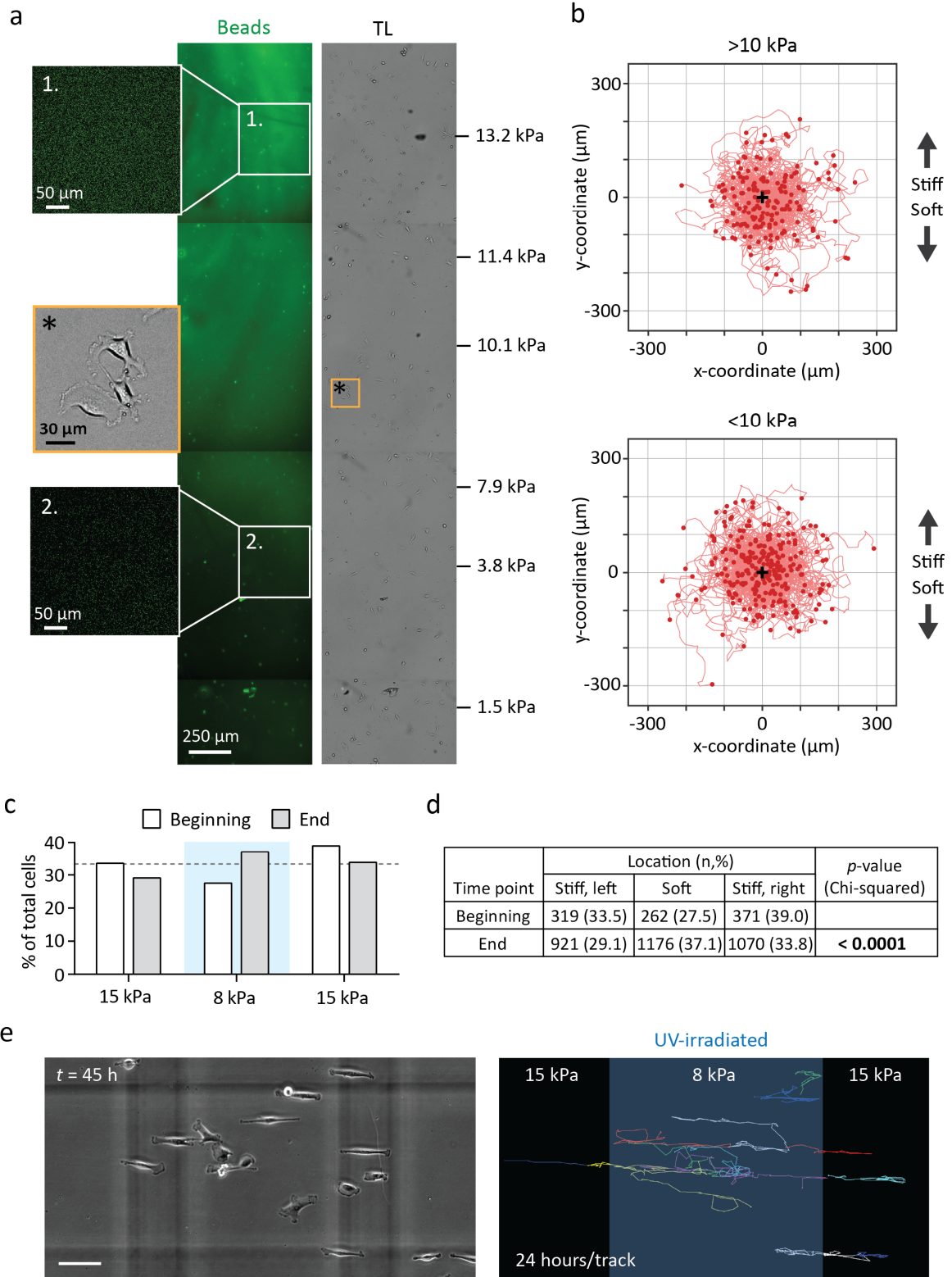
29

30 Figure S1. Preparation of diffusion-based stiffness gradient hydrogels. (a) Schematic
31 representation of stiffness gradient preparation. Two acrylamide solutions are polymerized and
32 mixed together on a glass bottom dish to create a continuous gradient in the range of 0.5–22
33 kPa. The hydrogel is activated and functionalized with fibronectin before use. (b) Calibration
34 curve connecting fluorescent marker bead density, measured using a confocal microscope, to the
35 elastic modulus of the hydrogel. Adapted from Ref.³¹ (c) Fibronectin density across the stiffness
36 gradient hydrogels, measured via immunofluorescence. Green, orange and blue colors denote
37 measurements from three individual experiments, overlaid with binned data. Squares depict
38 measurements from secondary controls, stained by omitting the anti-fibronectin antibody. Mean
39 \pm SD of $n = 19\text{--}86$ (anti-FN) or $9\text{--}42$ (control) regions of interest (ROIs).

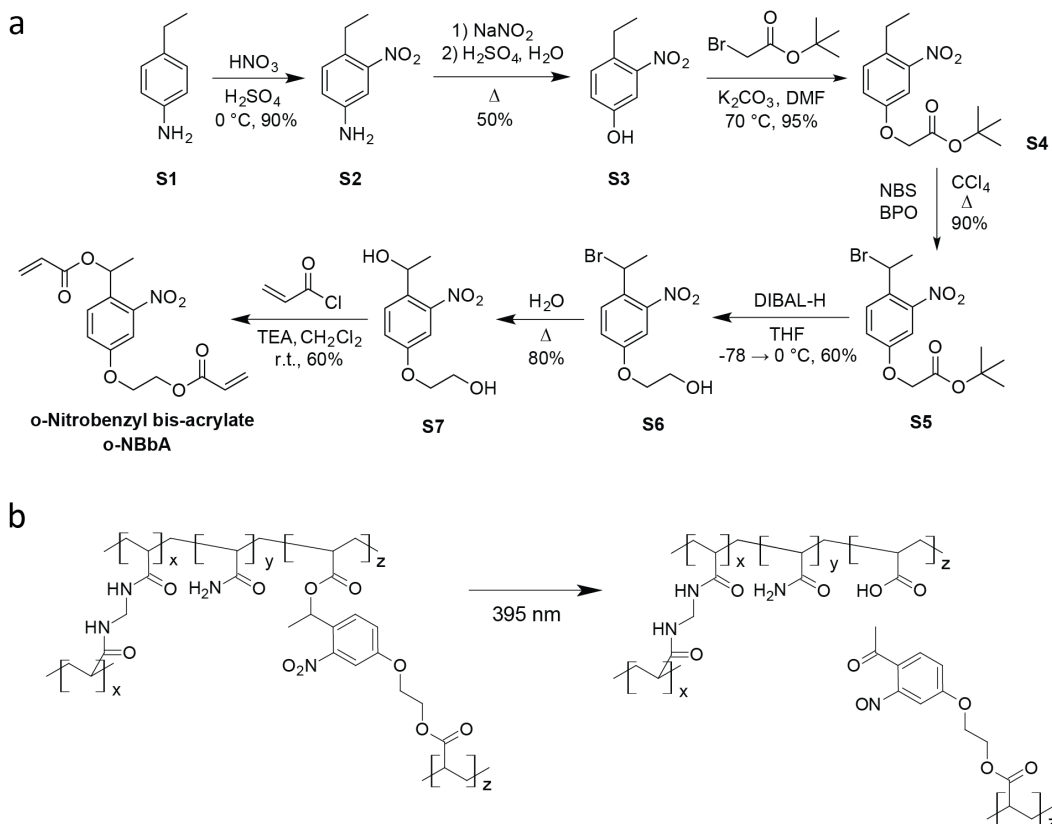


40

41 Figure S2. Mechanosensitivity of U-251MG proliferation. (a–b) Fluorescence images (a) and
42 quantification (b) depicting EdU incorporation by U-251MG cells on 0.5–60 kPa substrates. Scale
43 bar, 20 μ m. Mean values from three independent experiments. Analyzed by one-way ANOVA and
44 Sidak's *post hoc* test.

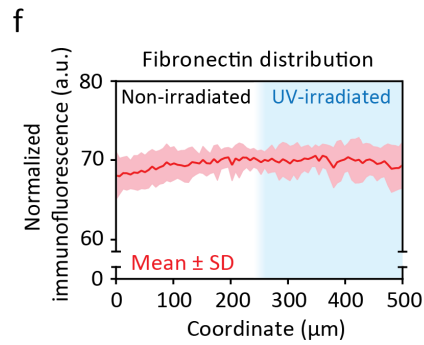
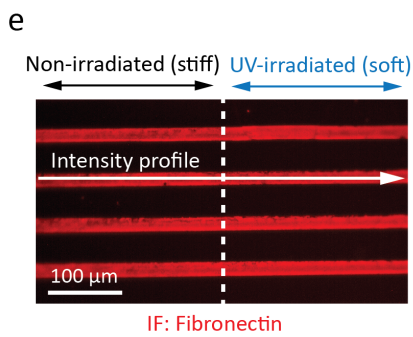
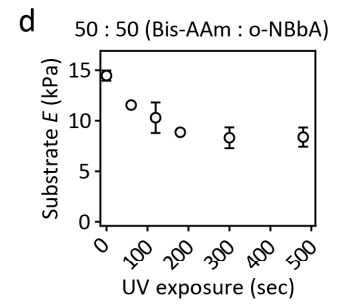
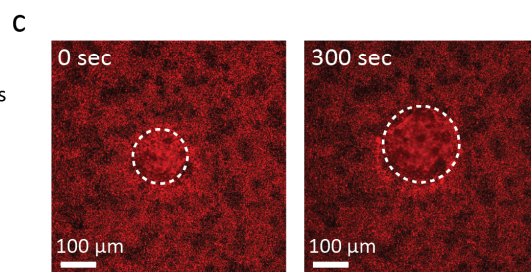
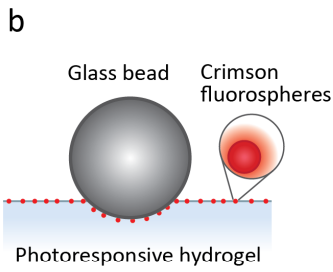
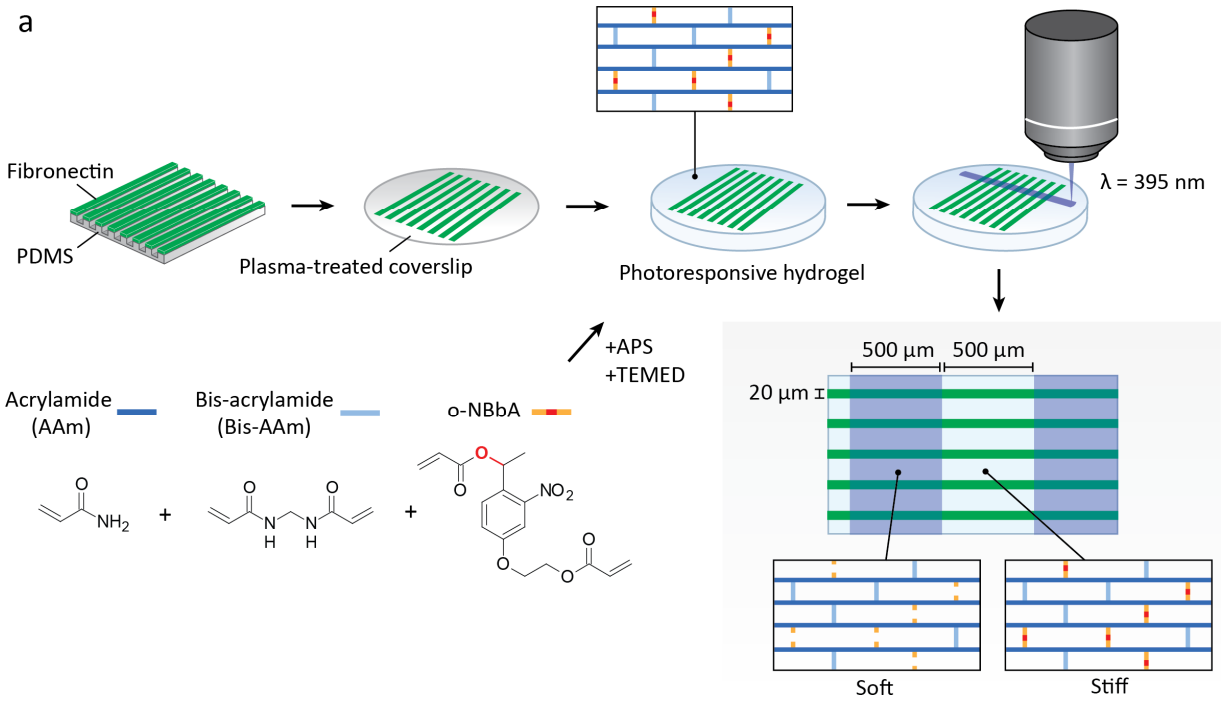


46 Figure S3. Tracking individual U-251MG cells on stiffness gradients. (a) Representative
47 fluorescence image of a stiffness gradient hydrogel (left) and live U-251MG cells adhering to the
48 substrate (right). (Insets 1, 2) Example confocal images of fluorescent beads, acquired as
49 described in Ref.³¹ The images correspond to the indicated gradient regions and were used for
50 calculating the substrate elastic moduli. (*) Close up of the cells. (b) Tracks from individual U-
51 251MG cells migrating on the stiffer (>10 kPa, top) and softer (<10 kPa, bottom) regions of a 0.5–
52 22 kPa stiffness gradient for 10 hours. The tracks correspond to the data in Fig. 1d and the origo
53 (0, 0) is highlighted by a black (+). n = 174–264 cells per condition, from three independent
54 experiments. (c–d) Total number of cells in the different gradient regions in Fig. 1f–g. (c) Bar
55 graph, n = 952–3,167 cells per time point, from two individual experiments. (d) Contingency table
56 summarizing the data, analyzed by chi-squared test. (e) Endpoints (left) and 24-hour tracks (right)
57 depicting the migration of individual cells on the photoresponsive stiffness gradients. Scale bar,
58 100 μm .

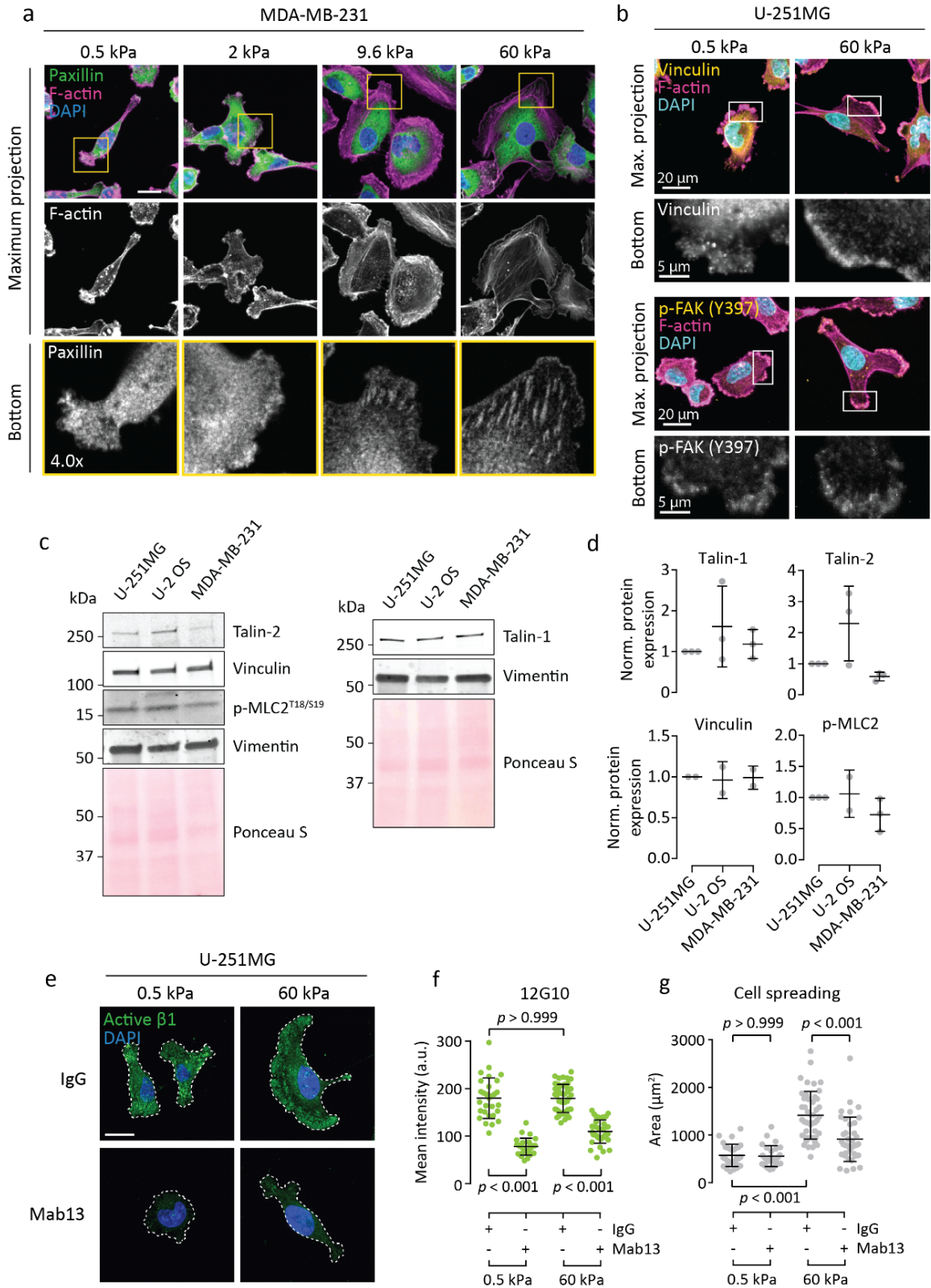


59

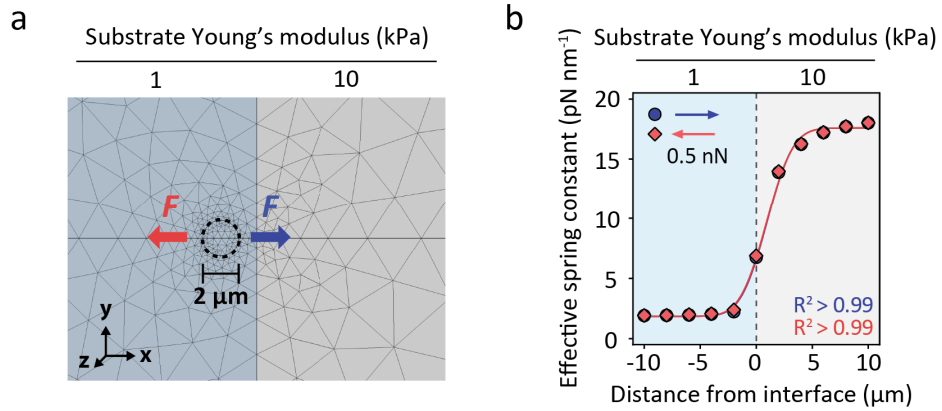
60 Figure S4. Synthesis and photochemistry of o-nitrobenzyl bis-acrylate. (a) Schematic of the
 61 synthesis of o-NBbA. (b) Copolymerization of o-NBbA with acrylamide and bis-acrylamide yields
 62 hydrogels composed of strands of polyacrylamide crosslinked by either o-NBbA or bis-
 63 acrylamide. UV irradiation cleaves the photolabile o-NBbA, resulting in gels with lower
 64 crosslinking density and hence lower stiffness. The process does not release any byproducts to
 65 the gel environment.



67 Figure S5. Preparation and characterization of photoresponsive hydrogels. (a) Schematic
68 representation of stiffness gradient preparation for migration experiments. The photocleavable
69 carbon-oxygen bond in o-NBbA is indicated by red color. **(b–d)** Stiffness characterization by bead
70 indentation. A schematic representation of the technique (b), representative fluorescence
71 images (c) and quantified results (d) depicting hydrogel elasticity as a function of UV exposure.
72 Dashed lines highlight indented, out-of-focus areas in the gel. Mean \pm SD of n = 3 measurements.
73 **(e–f)** Validation of the microcontact printed fibronectin patterns. Immunofluorescence image (e)
74 and quantification (f) showing fibronectin distribution on non-irradiated and UV-exposed regions
75 of the hydrogel. Mean \pm SD of n = 24 intensity profiles.

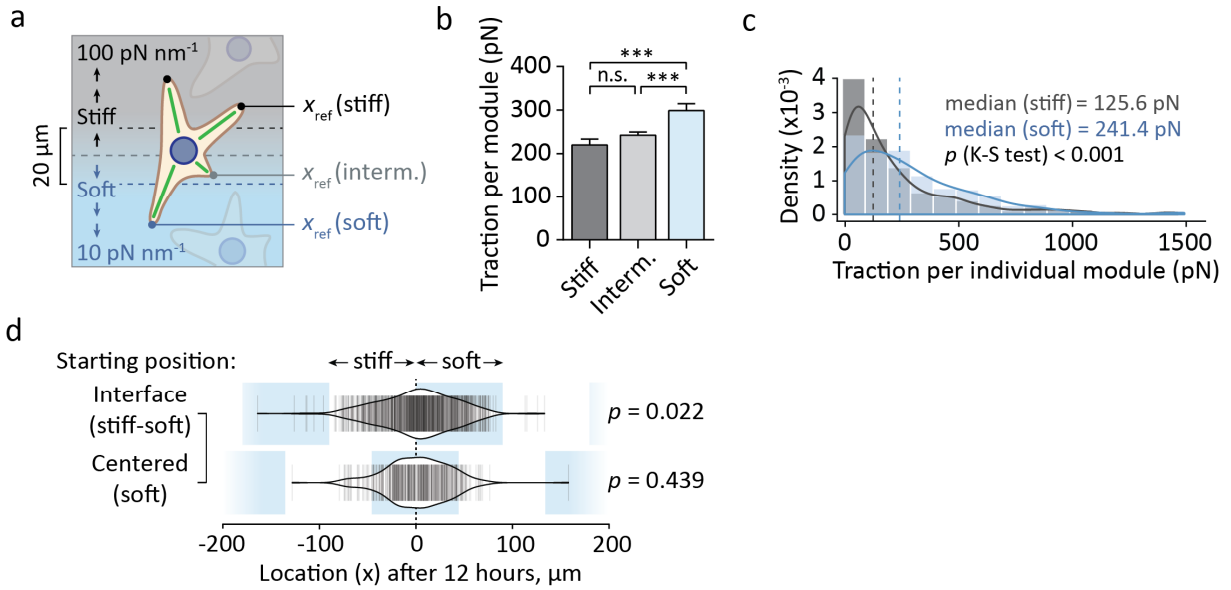


77 Figure S6. Focal adhesion maturation and adhesion components in U-251MG and other cancer
78 cells. (a) Immunofluorescence images of paxillin and F-actin in MDA-MB-231 cells on 0.5–60 kPa
79 substrates. The bottom panels show individual focal planes from confocal stacks, corresponding
80 to the basal side of each cell. Scale bar, 20 μ m. (b) Immunofluorescence images of vinculin (top),
81 p-FAK (bottom) and F-actin in U-251MG cells on 0.5 and 60 kPa substrates. The bottom panels
82 show individual focal planes from confocal stacks, corresponding to the basal side of each cell.
83 (c–d) Representative western blots (c) and quantification (d) depicting talin-1/2, vinculin and p-
84 MLC2 levels across three different cell lines. Densitometric measurements were normalized to
85 vimentin, mean \pm SD of 2–3 independent experiments. (e–f) Immunofluorescence images (e) and
86 quantification (f) showing active β 1-integrin (clone 12G10) in U-251MGs on 0.5 and 60 kPa
87 substrates. The cells were treated with a control antibody (normal rat IgG) or β 1 function-
88 blocking Mab13 for two hours before fixation. Scale bar, 20 μ m. Mean \pm SD of n = 27–45 cells,
89 analyzed by Kruskal-Wallis one-way ANOVA and Dunn's *post hoc* test. Representative of two
90 independent experiments. (g) Spreading of U-251MGs on 0.5 and 60 kPa substrates, without or
91 after β 1-integrin blocking by Mab13. Mean \pm SD of n = 27–45 cells, analyzed by Kruskal-Wallis
92 one-way ANOVA and Dunn's *post hoc* test. Representative of two independent experiments.



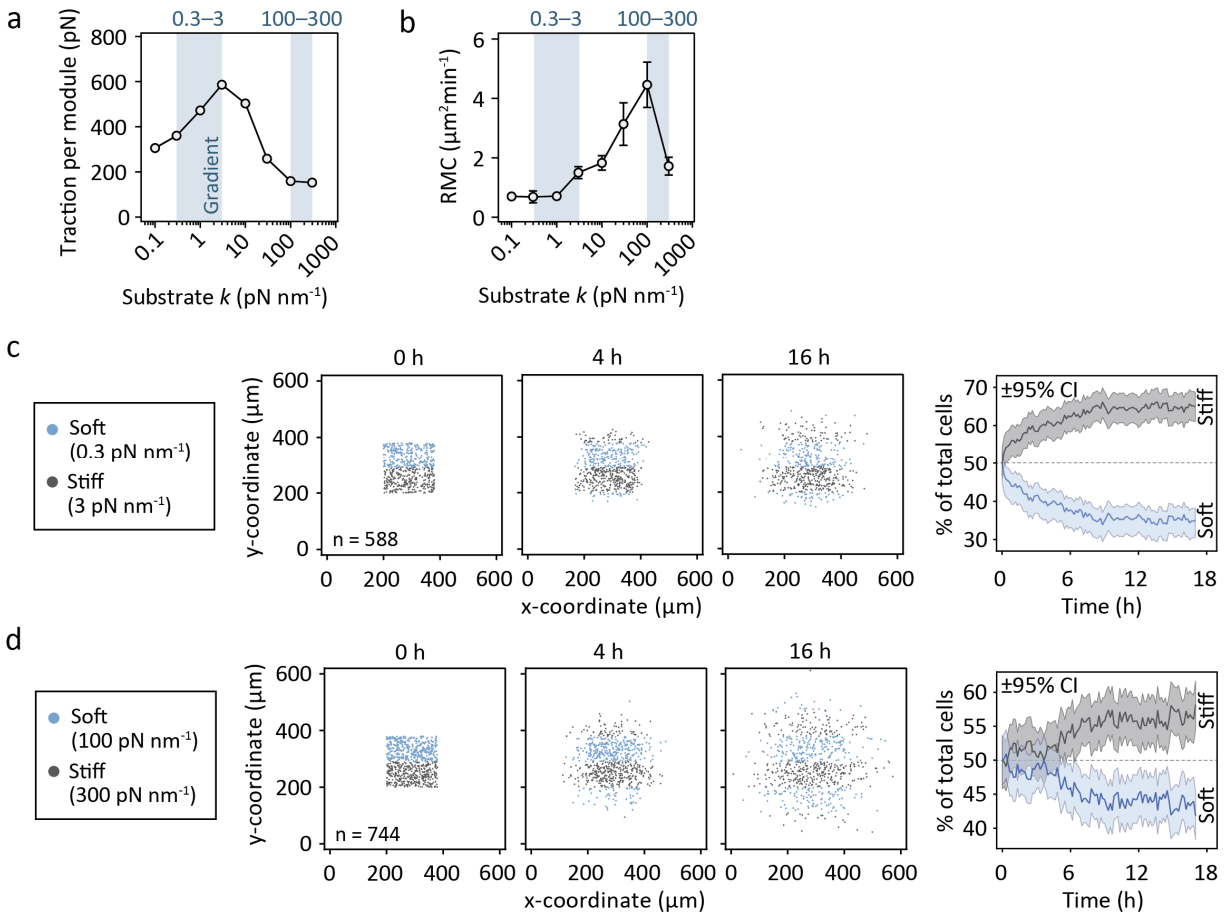
93

94 Figure S7. Finite element analysis of polyacrylamide displacement next to a stepwise elastic
95 gradient. (a) COMSOL Multiphysics® model setup (b) The effect of steep elastic gradients on the
96 effective spring constant of polyacrylamide. A lateral 0.5 nN force was exerted on the substrate
97 through a circular adhesion zone ($r = 1 \mu\text{m}$) as shown in (a). The position of the adhesion zone
98 was adjusted repeatedly at $2 \mu\text{m}$ steps. The direction of the force was varied by 180° but was
99 always parallel to the gradient. In both cases, normal cumulative distribution function was a good
100 fit to the data.



101

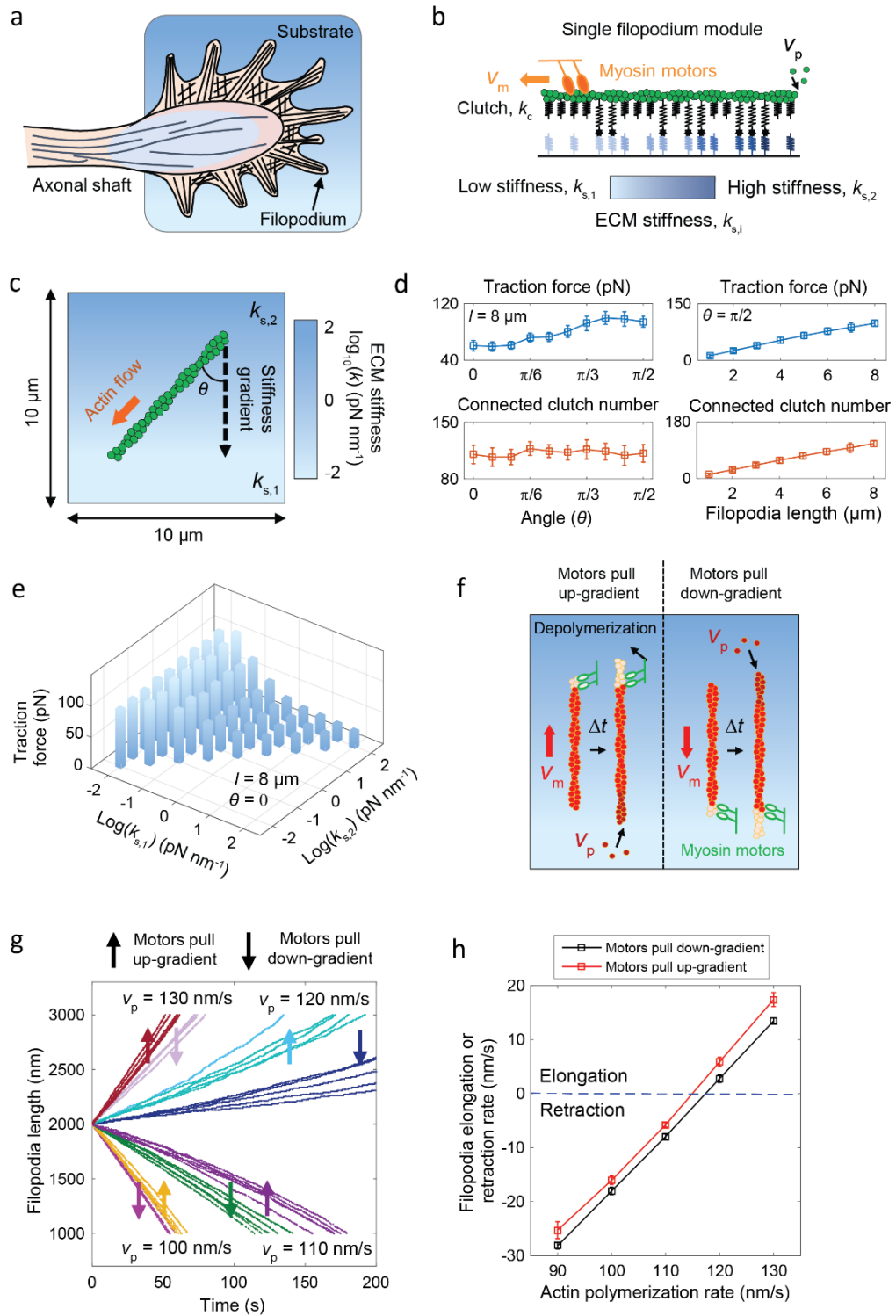
102 Figure S8. CMS produces asymmetric traction forces in cells that interact with stiffness
 103 gradients. (a) When individual cells were on top of a stiffness gradient during the simulations in
 104 Fig. 3b–f, their traction forces were recorded. (b–c) Forces exerted by clutch modules on stiff,
 105 intermediate and soft substrate, while the cell body is located on a stiffness gradient. (b) Bar
 106 graphs depicting mean ± SEM of n = 292–1380 modules. ***p < 0.001, n.s. = not significant,
 107 Kruskal-Wallis one-way ANOVA and Dunn's *post hoc* test. (c) Histograms overlaid with probability
 108 density functions, dashed lines indicate medians. n = 292–365 modules, analyzed by Kolmogorov-
 109 Smirnov test. (d) Violin plots of accumulated distance migrated by individual cells along the
 110 orientation of the gradient and over 12 hours, starting from a gradient (top) or from the middle
 111 of a compliant region (bottom). n = 326–759 cells, analyzed by sign test.



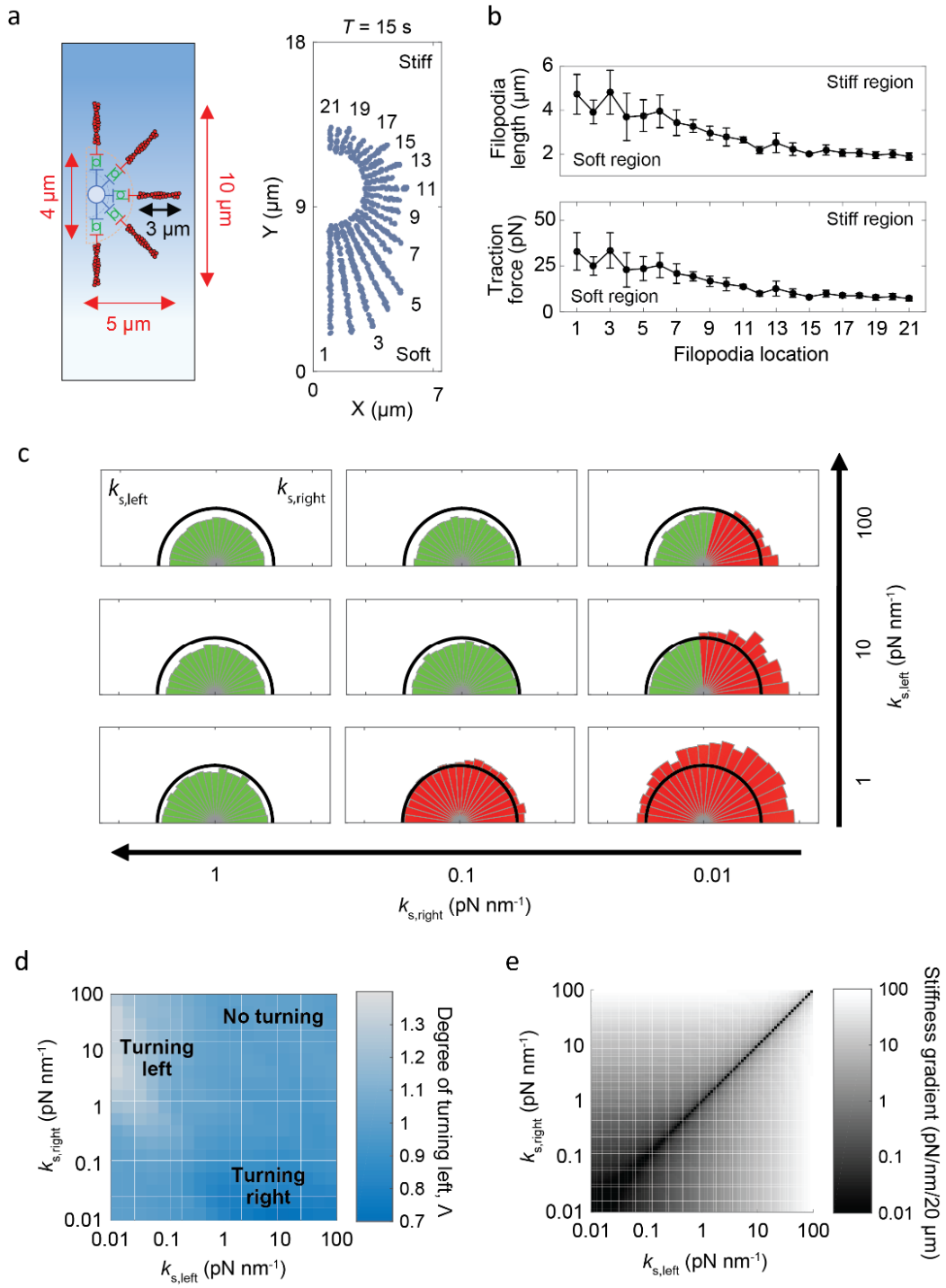
112

113 Figure S9. Modifying the range of the stiffness gradient can reverse durotaxis *in silico*. (a–b)
 114 Module traction forces (a) and RMC (b) of the simulated cells as a function of substrate stiffness,
 115 as in Fig. 3c–d. Overlays highlight the ranges of the 0.3–3 pN nm^{-1} and 100–300 pN nm^{-1} gradients
 116 in (c–d). Mean \pm SEM of $n = 10$ cells. (c–d) Evolution of cell density on mechanically
 117 heterogeneous substrates over time. (c) Coordinates of individual cells on the 0.3–3 pN nm^{-1}
 118 gradient 0, 4 and 16 hours into the simulation (left) and the fraction of cells residing in the stiffer
 119 and softer areas over the course of the simulation (right). $\pm 95\%$ CI, $n = 588$ cells. (d) As above,
 120 but for the 100–300 pN nm^{-1} gradient. $n = 744$ cells.

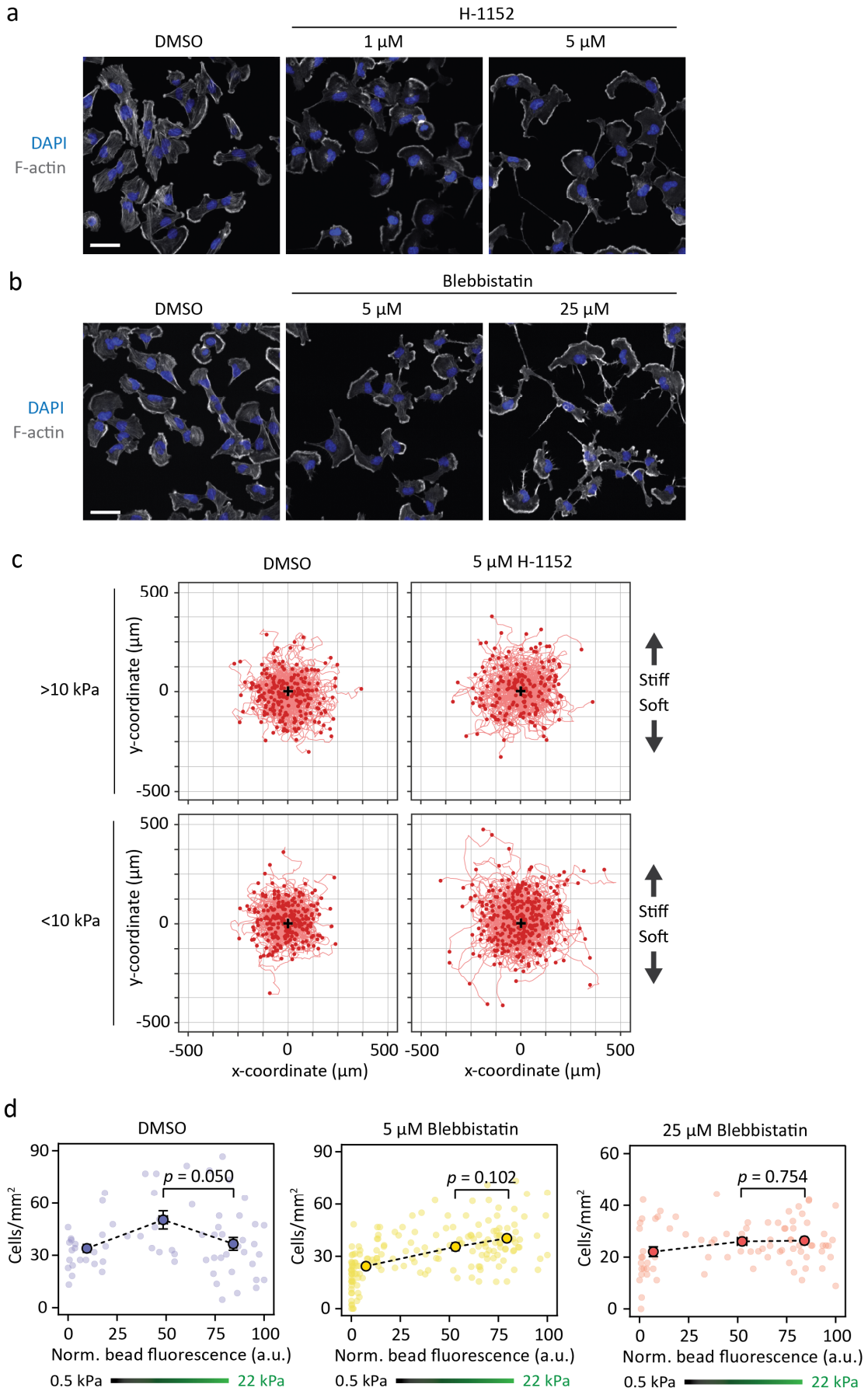
Isomursu et al., Figure S10.



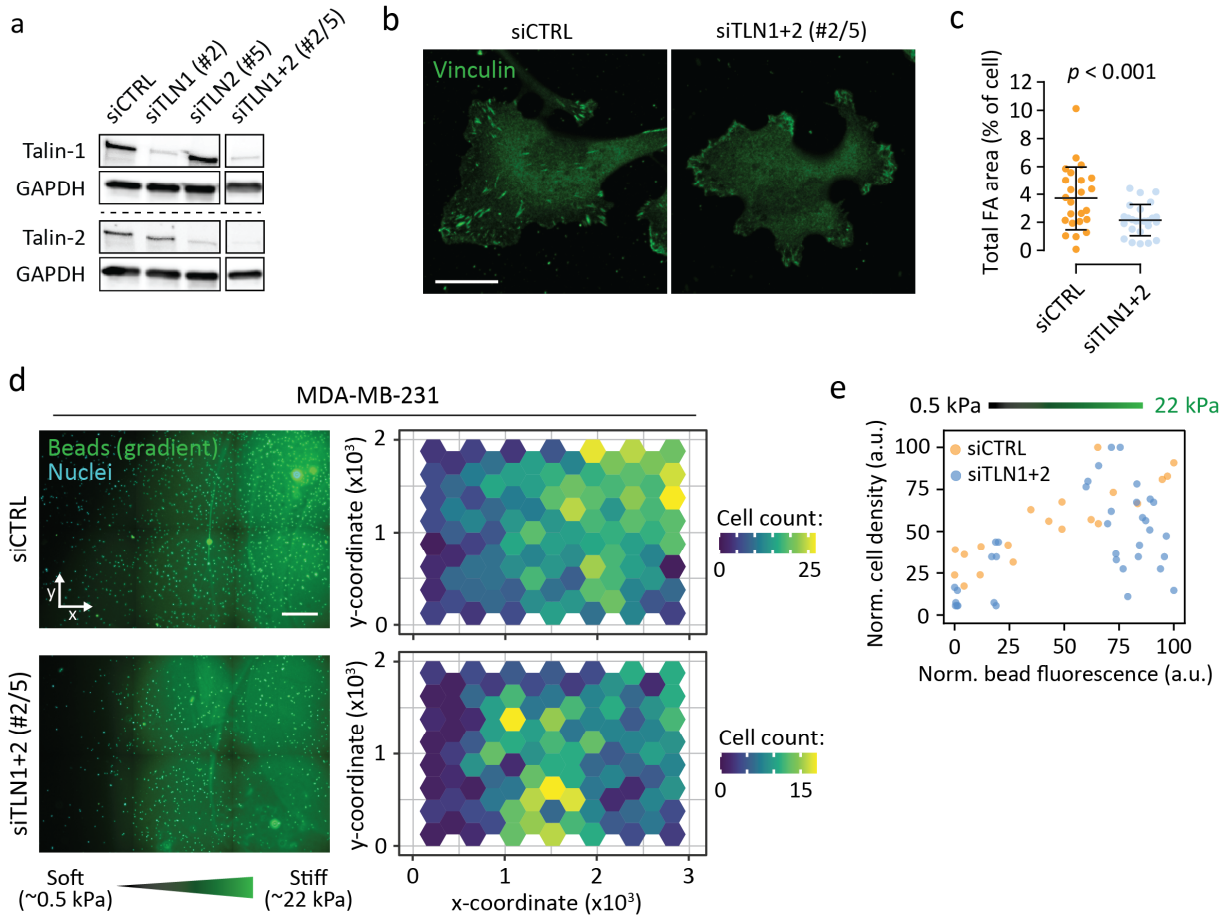
122 Figure S10. Motor-clutch model of filopodial dynamics. (a) Schematic representation of a
123 neuronal GC. Filopodia, surrounded by a less polarized actin network, reside in the peripheral
124 domain. They are separated from the axon by a thin transitional domain, and a central domain
125 (light blue) that is primarily composed of microtubules. (b) The filopodia in GCs are modeled as
126 individual motor-clutch modules, with adhesion springs (homogeneous stiffness), substrate
127 springs (heterogeneous stiffness) and inward actin flow resulting from active myosin motors.
128 Actin monomers are added into the filaments at a constant rate. (c) Setup used in the single-
129 filopodium simulations. The filopodium interacts with the substrate in a set orientation relative
130 to the linear stiffness gradient. (d) (Left) Traction force exerted by the filopodium increases when
131 the protrusion is pointing down the gradient, toward softer substrate. (Right) Perpendicular to
132 the gradient, traction increases with filopodia length mainly due to more clutches being available
133 to bind with the substrate. Data shown are from $n = 10$ independent simulations. (e) Average
134 traction exerted by a single filopodium on different substrate stiffness gradients. Data represent
135 means of $n = 10$ simulations. (f) Filopodia length is affected by both actin flow, v_m , and the
136 polymerization rate, v_p . Depending on the orientation of the filopodium, the actin may flow
137 toward soft (filopodium pointing up the gradient) or stiff (filopodium pointing down the gradient)
138 substrate. (g) Evolution of filopodia length on stiffness gradients upon different actin
139 polymerization rates. The different combinations of v_p and filopodia orientation are color-coded,
140 while each line represents the temporal variation in the length of a single filopodium. (h) Effect
141 of actin polymerization and orientation relative to a stiffness gradient on the filopodia
142 elongation/retraction rate. Mean \pm SEM in (d) and (h).



144 Figure S11. Motor-clutch model predicts growth cone steering toward soft matrix. (a)
145 Schematic representation of the GC model. (Left) Dimensions of a newly initialized GC. (Right)
146 Each GC consists of multiple filopodia, distributed between $-\pi/2$ and $\pi/2$ relative to the axon. On
147 stiffness gradients ($k_{s,1} = 0.01 \text{ pN nm}^{-1}$, $k_{s,2} = 100 \text{ pN nm}^{-1}$), filopodia on the more compliant side
148 of the substrate rapidly outgrow the others, leading to effective turning of the GC. (b) Filopodia
149 length (top) and traction (bottom) based on their orientation around the GC central domain. On
150 stiffness gradients, filopodia pointing toward the softer substrate elongate faster and generate
151 more traction. Data shown are from $n = 10$ independent simulations. (c) Examples of GC behavior
152 on different stiffness gradients. Green denotes filopodia that are retracting during the course of
153 the simulation, red denotes filopodia that are elongating. Depending on the gradient, individual
154 GCs may retract or enlarge isotropically, or steer toward the softer substrate. Displayed are
155 means of $n = 10$ simulations. (d) Phase diagram of GC turning to left, Δ , on different mechanically
156 graded substrates. (e) Phase diagram depicting the strength of the stiffness gradient for varying
157 $k_{s,1}$ and $k_{s,2}$. Gradient strength alone cannot explain the magnitude of Δ , if the whole substrate
158 is stiffer than the optimal range for individual filopodia (Fig. S7e).

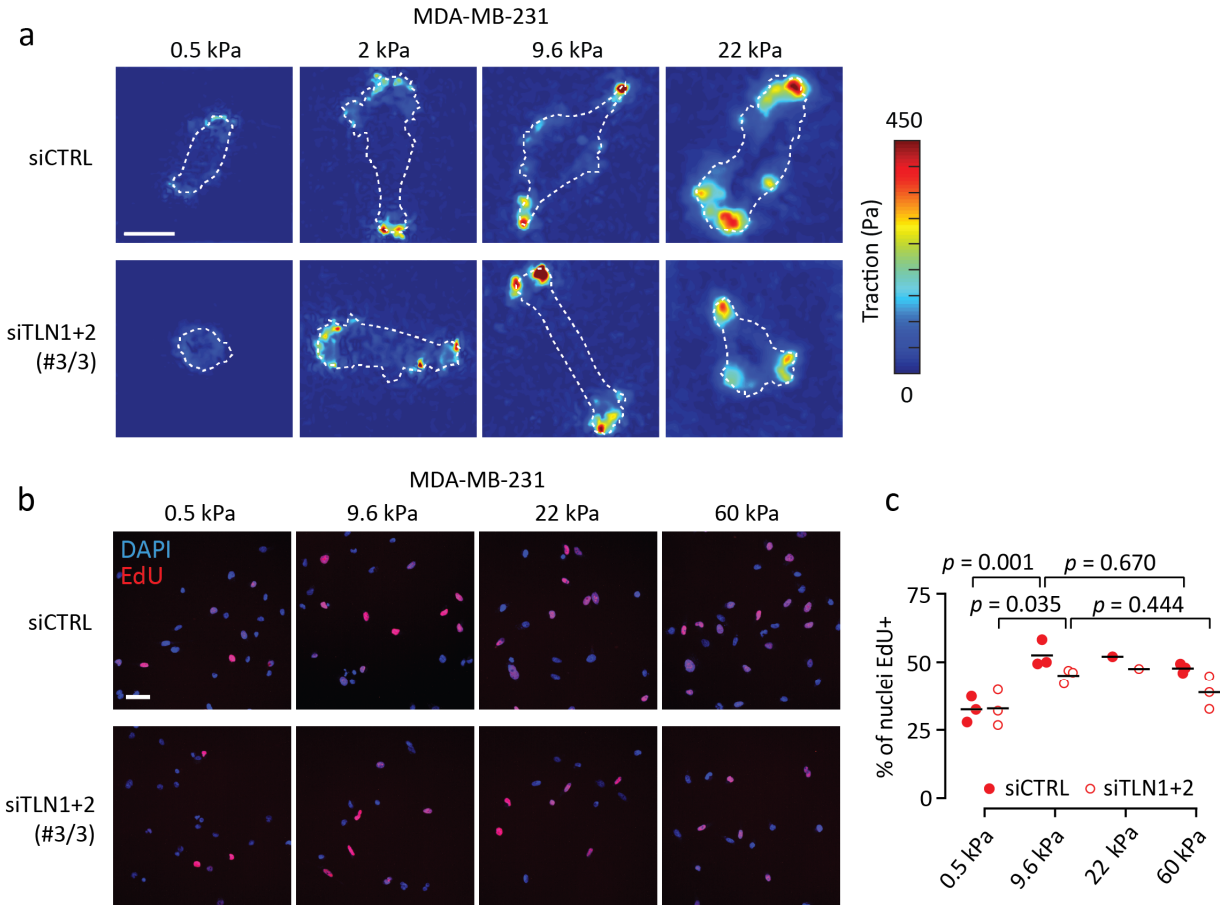


160 Figure S12. Morphology and migration of U-251MG cells during ROCK and myosin II inhibition.
161 (a–b) Validation of different actomyosin-targeting compounds using U-251MG cells.
162 Fluorescence images of the actin cytoskeleton after treatment with intermediate and high doses
163 of ROCK inhibitor H-1152 (a) or myosin II inhibitor blebbistatin (b) for two hours. Scale bar, 50
164 μm . (c) Tracks from individual U-251MG cells migrating on the stiffer (>10 kPa, top) and softer
165 (<10 kPa, bottom) regions of a 0.5–22 kPa stiffness gradient for 10 hours, treated with 5 μM H-
166 1152 or vehicle (DMSO). The tracks correspond to the data in Fig. 4g and each origo (0, 0) is
167 highlighted by a black (+). $n = 177\text{--}327$ cells per condition, from one (DMSO) to two (H-1152)
168 independent experiments. (d) Cell densities in different parts of 0.5–22 kPa gradients, 48 hours
169 after being seeded and supplemented with varying concentrations of blebbistatin. Mean \pm SEM
170 of $n = 13\text{--}85$ ROIs per bin, from two gradient hydrogels per condition, representative of two
171 independent experiments. Analyzed by Mann-Whitney test.



172

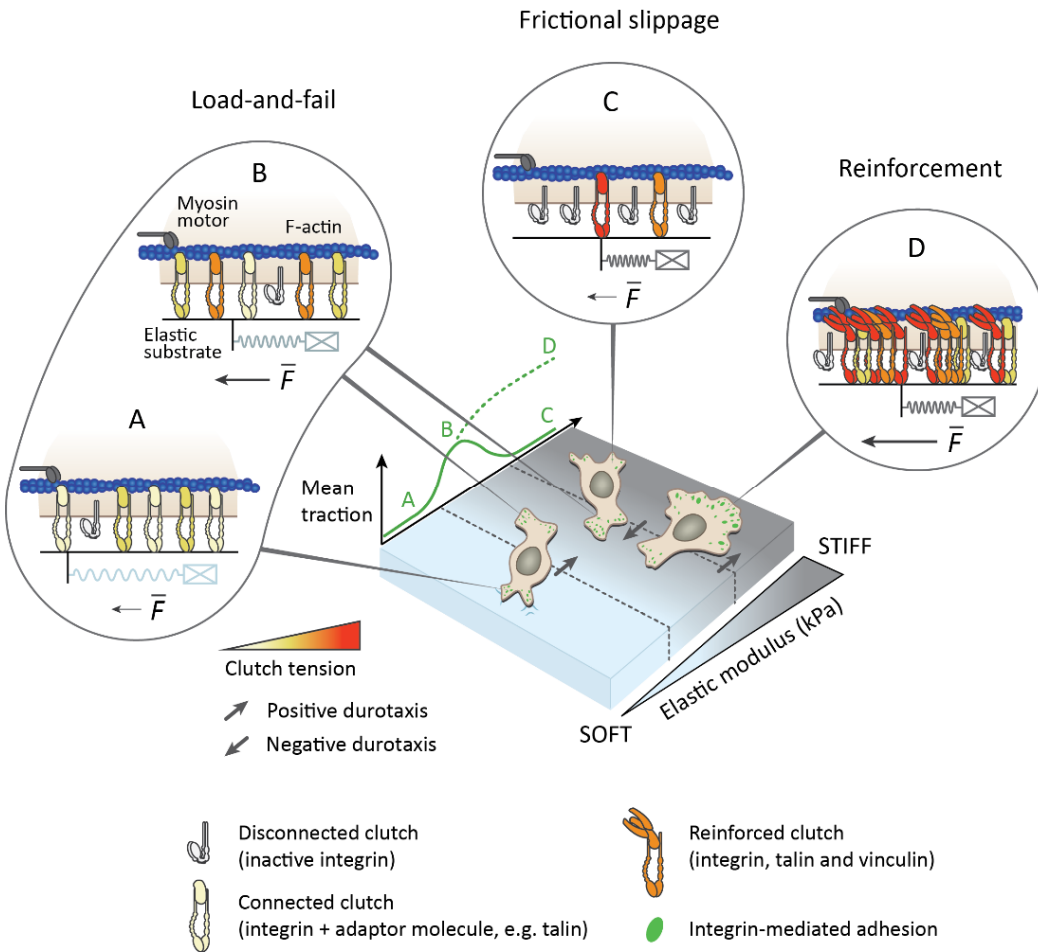
173 Figure S13. Additional talin-1/2-targeting siRNAs recapitulate the loss of mature adhesions and
 174 promote a switch from positive to negative durotaxis in MDA-MB-231 cells. (a) Representative
 175 western blot depicting talin-1 and talin-2 knockdown in MDA-MB-231 cells using siRNA oligos
 176 that are different from the ones used in Fig. 5. The fourth band on each row, depicting a double
 177 knockdown, was cropped from a different site in the same membrane. (b–c)
 178 Immunofluorescence images (b) and quantification (c) of vinculin-positive focal adhesions in
 179 MDA-MB-231s on 60 kPa substrate, without and after talin knockdown. Scale bar, 20 μm. Mean
 180 ± SD of n = 24–25 cells, analyzed by Mann-Whitney test. (d) (Left) Representative regions of two
 181 0.5–22 kPa polyacrylamide stiffness gradients, 72 hours after being seeded with MDA-MB-231
 182 cells. Scale bar, 500 μm. (Right) Quantification of cells across the gradients. (e) Relative MDA-MB-
 183 231 cell densities in different parts of the stiffness gradients. n = 20–36 ROIs, representative of
 184 two independent experiments.



185

186 Figure S14. Mechanosensitive traction and proliferation of MDA-MB-231 cells. (a)
 187 Representative traction maps from MDA-MB-231 cells on 0.5–22 kPa substrates, corresponding
 188 to the data in Fig. 5f. Cell outlines are indicated by white dashed lines. Scale bar, 20 μ m. (b–c)
 189 Fluorescence images (a) and quantification (b) depicting EdU incorporation by control and talin-
 190 low MDA-MB-231 cells on 0.5–60 kPa substrates. Scale bar, 50 μ m. Mean values from one to
 191 three independent experiments. Analyzed by one-way ANOVA and Sidak's *post hoc* test.

192



193

194 Figure S15. Schematic representation of the regulation of positive and negative durotaxis by
 195 motor-clutch dynamics. Cell-intrinsic molecular machinery dictates the cell's capacity to exert
 196 force on mechanically heterogeneous substrates, driving positive or negative durotaxis. Without
 197 clutch reinforcement (mechanosensitive FA formation, D), the motor-clutch model predicts a
 198 biphasic relationship between traction force and substrate stiffness (A–C)^{18,19,26–30}. This
 199 fundamental relationship, and the physical reinforcement of cell-matrix adhesion by FAs, are
 200 likely to be further influenced by biochemical signaling pathways and feedback loops that
 201 modulate the expression, activity and localization of individual cytoskeletal and clutch
 202 components, in a cell type-dependent manner.

203 Supplementary Text 1: Chemistry of o-NBbA and photoresponsive polyacrylamide
204 hydrogels

205 Polyacrylamide was selected as the base material for the stiffness gradients used in this study, as
206 it is the most widely employed model system for investigating the role of substrate stiffness in
207 directing cell behavior. This is partly due to the ease of obtaining elastic moduli in a wide,
208 physiologically relevant range^{51,52}. While other types of gels (e.g. collagen or hyaluronic acid) are
209 known to interact directly with cell surface receptors, including integrins, polyacrylamide gels are
210 inert to such interactions. This allows more control over the types and densities of ligands that
211 will be presented to the cells, making the material ideal for mechanobiological studies. Various
212 methods have been developed to fabricate stiffness gradients in gels to study the durotactic
213 behavior of cells. Some examples exploit the diffusion of two prepolymer solutions^{13,31}, tilted-
214 superposition of two hydrogels⁵³, freeze-thaw-induced crosslinking of polyvinyl alcohol⁵⁴, or
215 toehold-mediated strand displacement of DNA⁵⁵. Aiming for high-resolution spatiotemporal
216 control over the mechanical properties of the gel, we chose light as the external stimulus⁵⁶⁻⁶⁰.
217 Therefore, we aimed to design and synthesize a new, minimalistic and photocleavable crosslinker
218 that contains acrylate moieties.

219 Among various photolabile functionalities that are available, o-nitrobenzyl (o-NB) was chosen
220 due to its high one-photon photolysis efficiency and high deprotection yields^{61,62}. o-NB based
221 compounds have been used widely in hydrogel-based studies to achieve controlled release or
222 immobilization of payloads⁶³⁻⁶⁷, photodegradation of gels⁶⁸⁻⁷⁰, or modulation of gel stiffness^{58,71}.
223 However, many of these studies have focused on polyethylene glycol-based gels rather than
224 polyacrylamide, or complete degradation of the gel rather than controlling the Young's modulus.
225 To our knowledge, there has been only one report to date where o-NB-based crosslinkers have
226 been used to fabricate photoresponsive polyacrylamide hydrogels⁷². While the study
227 demonstrates the feasibility of o-NB based crosslinking, the method itself requires multiple steps
228 to crosslink chains of polyacrylamide through the o-NB moiety, which made its application here
229 unwieldy.

230 In this study, a simple one-step synthesis of photoresponsive polyacrylamide gels was enabled
231 by the functionalization of an o-NB group with two acrylate moieties to yield a crosslinker that
232 would cleave upon photolysis. The photocleavable crosslinker, o-nitrobenzyl bis-acrylate (o-
233 NBbA), was synthesized in seven steps from p-ethyl aniline (Fig. S4a) and designed so that its
234 cleavage would not release any byproducts in the medium (Fig. S4b). Based on a previously
235 reported polyacrylamide recipe⁴⁶, a photoresponsive gel with an initial stiffness of 20 kPa that
236 can be reduced down to 10 kPa was designed by replacing 50 mol % of bis-acrylamide with o-
237 NBbA. The resulting gel exhibited a Young's modulus of ~15 kPa that was reduced down to ~8
238 kPa after complete cleavage of the o-NBbA crosslinker by exposure to 395 nm light for 5 min (Fig.

239 S5b–d). The slight discrepancy between the expected and measured substrate stiffness could be
240 due to the relatively low water solubility and partial phase separation of o-NBbA in the
241 prepolymer solution, which would result in softening of the hydrogel post-polymerization⁷³.

242 The light source used for the photocleavage was an LED from a SpectraX light engine instrument
243 installed in a Nikon TiE microscope, originally intended for epifluorescence imaging. This method
244 had several advantages: spatial control can be achieved easily, as the location of the substrate
245 can be precisely chosen via phase-contrast imaging and the area of irradiation can be controlled
246 with the field diaphragm and objectives. For instance, the diameter of the LED-irradiated area
247 could be adjusted to as low as 59 μm using a 40x objective with a nearly closed field diaphragm,
248 or as high as 978 μm under a 10x objective with a fully opened field diaphragm. Stiffness patterns
249 could also be created using the ‘time lapse movie’ function of the NIS-Elements software (Nikon).
250 Here, alternating stiffness gradients were created by initiating a time-lapse movie between two
251 regions of the gel, a method that could be modified to yield more complex 1D patterns or even
252 2D shapes. Although not explored here, temporal control would be equally possible: for example,
253 stiffness gradients could be introduced in gels at various time points during live cell culture, while
254 simultaneously observing cellular behavior and responses.

255 To conjugate fibronectin to the surface of the gel via covalent interaction, acrylic acid N-
256 hydroxysuccinimide (NHS) ester was used as the tethering agent. While two methods, addition
257 of acrylic acid NHS ester in the pregel solution followed by stamping of fibronectin, or stamping
258 of the pregel solution with fibronectin preincubated with acrylic acid NHS ester, both produced
259 fibronectin-patterned hydrogels, the former was chosen since it yielded more consistent results.
260 Once the gel had been fabricated, any remaining NHS ester moieties in the gel were passivated
261 with bovine serum albumin (BSA) in PBS to prevent any non-specific interactions between the gel
262 and cells.

263 Supplementary Text 2: Implementation of the cell migration simulator using
264 mechanically heterogeneous substrates

265 To establish whether our observations of negative (and positive) durotaxis could be explained
266 through a single set of principles, namely the motor-clutch dynamics of cell-matrix adhesions, we
267 developed a modified version of the cell migration simulator (CMS) that can be used for modeling
268 cell migration on mechanically heterogeneous substrates. The detailed governing equations and
269 algorithms of the original CMS were described previously²⁹. Briefly, the CMS comprises multiple
270 motor-clutch models (i.e. modules) that mimic cellular protrusions found in U-251MG
271 glioblastoma cells over the stiffness range used in the study. These include multiple lamellipodial
272 protrusions distributed at the leading edge and around the perimeter of the migrating cell (Fig.
273 2c, Ref.²⁹). Cell motion is determined by a force balance between the modules and a central cell
274 body (Fig. 3a). In the CMS, new modules are nucleated stochastically, module length increases
275 over time via actin polymerization that is simultaneously counteracted by myosin-induced
276 retraction of actin fibers, and modules are removed when they become too short. In addition,
277 total actin and numbers of clutches and motors are kept constant in accordance with the
278 conservation of mass.

279 In each motor-clutch system, adhesion clutches bind to elastic substrate springs with a constant
280 rate of k_{on} . Connected clutches form a direct mechanical link from the intracellular cytoskeleton
281 to the extracellular substrate – forces are borne from active myosin motors and transmitted by
282 the resulting inward actin flow. The unbinding rate of a connected clutch i , $k_{off,i}$, varies with
283 force F_i according to the Bell model⁷⁴:

$$k_{off,i} = k_{off}^* \exp(F_i/F_b) \quad (S1)$$

$$F_i = k_c x_i$$

284 where k_{off}^* is the clutch unbinding rate in the absence of loading, F_b is the characteristic clutch
285 rupture force, and x_i is the elongation of the spring representing the i^{th} connected clutch with a
286 spring constant k_c . The actin filaments are pulled by n_m myosin motors, each capable of exerting
287 a force F_m , and balanced by the traction force F_s , resulting in inward actin flow with the effective
288 actin flow rate (v_m) based on

$$v_m = v_m^* \left(1 - \frac{F_s}{F_{stall}} \right) \quad (S2)$$

289 where v_m^* is the unloaded rate, $F_{stall} = n_m F_m$ is the stall force of the ensemble of myosin
290 motors, and the traction force F_s transmitted by all the connected clutches is given by:

$$F_s = \sum_{i=1}^{n_{c,on}} F_i \quad (S3)$$

291 in which $n_{c,on}$ is the number of connected clutch bonds. Actin monomers are added to the
 292 barbed ends of actin filaments in the cellular protrusions (modules) at a polymerization rate v_p ,
 293 constrained by the total actin length A_{tot} in the cell according to the relation:

$$v_p = v_p^*(A_{free}/A_{tot}) \quad (S4)$$

294 where A_{free} is the amount of available G-actin and v_p^* is the maximum polymerization rate.
 295 Module elongation and retraction both result from this actin polymerization and the actin flow
 296 rate (v_m). New modules are nucleated at a nucleation rate k_{mod} , also constrained by actin
 297 availability:

$$k_{mod} = k_{mod}^*(A_{free}/A_{tot}) \quad (S5)$$

298 where k_{mod}^* is the maximum module nucleation rate. Actin filaments are depolymerized into
 299 actin monomers when they pass through the position of the myosin motors. Filaments can also
 300 be capped and polymerization arrested by actin capping proteins at a capping rate k_{cap} . Actin
 301 filaments, and the corresponding modules, are removed from the simulation when their length
 302 falls below l_{min} .

303 Monte Carlo simulations were conducted using a direct Gillespie Stochastic Simulation
 304 Algorithm⁵⁰, with each time step determined based on total event rates, including k_{on} , $k_{off,i}$,
 305 k_{mod} , and k_{cap} , and the event execution determined based on accumulated event rates. The
 306 CMS C++ version, described in³⁸, was modified to account for variations in substrate stiffness
 307 (described below), and simulations were conducted in Mesabi computer cluster at the Minnesota
 308 Supercomputing Institute (MSI).

309 After the simulated cells had reached a dynamic steady state (60 min), they were displaced
 310 randomly to a 180 μm x 180 μm region (Fig. 3b), and the substrate stiffnesses (k_s) experienced
 311 by the cell body and each protrusion were determined based on their respective y-coordinates
 312 (y). The substrate could be either soft (k_{soft}), stiff (k_{stiff}), or between the two extremes [gradients
 313 following a normal cumulative distribution function, described by the following error functions
 314 (erf)]:

$$k_s = k_{soft} \quad -\frac{1}{2}\Delta y_{gradient} - \Delta y_{plateau} < y \leq -\frac{1}{2}\Delta y_{gradient} \quad (S6)$$

$$k_s = k_{soft} + \frac{1}{2}(1 + \text{erf}(4y/\Delta y_{gradient})) (k_{stiff} - k_{soft}) \quad -\frac{1}{2}\Delta y_{gradient} < y \leq \frac{1}{2}\Delta y_{gradient} \quad (S7)$$

$$k_s = k_{stiff} \quad \frac{1}{2}\Delta y_{gradient} < y \leq \frac{1}{2}\Delta y_{gradient} + \Delta y_{plateau} \quad (S8)$$

$$k_s = k_{\text{stiff}} + \frac{1}{2} \left(1 + \operatorname{erf} \left(4 \frac{y - \Delta y_{\text{gradient}} - \Delta y_{\text{plateau}}}{\Delta y_{\text{gradient}}} \right) \right) (k_{\text{soft}} - k_{\text{stiff}}) \quad \frac{1}{2} \Delta y_{\text{gradient}} + \Delta y_{\text{plateau}} < y \leq \frac{3}{2} \Delta y_{\text{gradient}} + \Delta y_{\text{plateau}} \quad (\text{S9})$$

315 where $\Delta y_{\text{gradient}}$ is the width of a region with stiffness gradient (30 μm) and $\Delta y_{\text{plateau}}$ is the width
 316 of a region with constant stiffness (60 μm). This way, the number of cells in both soft and stiff
 317 regions was initially the same. In addition, by repeating the same stiffness pattern *ad infinitum*,
 318 the finite amount of cells placed in the finite rectangular region was representative of infinite
 319 cells placed on an infinite substrate with the same initial distribution of cells between soft and
 320 stiff areas. A normal cumulative distribution function was selected due to a finite element model
 321 of polyacrylamide, which demonstrated that the effective spring constant around a true stepwise
 322 gradient of elastic modulus follows a similar distribution (Fig. S7). This was valid regardless of the
 323 orientation of the applied traction (soft-to-stiff vs. stiff-to-soft).

324 Here, we adopted the high-motor-clutch parameter values used previously²⁹ to describe U-
 325 251MG migration on mechanically distinct but isotropic substrates (Table S2). Clutch stiffness
 326 was further adjusted to 8 pN nm^{-1} to better recapitulate the stiffness-dependence of U-251MG
 327 speed *in vitro*²⁹. Moreover, the total number of available molecular motors
 328 (N_m) was adjusted between 4,000 and 10,000 to evaluate the impact of actomyosin inhibition on
 329 the U-251MG stiffness optimum (Fig. 4a–b). During the CMS simulations, cell positions and
 330 traction forces were recorded every second. The data collected during the first 60 min were
 331 analyzed to ensure that the simulated cells had indeed reached a dynamic steady state. Random
 332 motility coefficients (RMC) were calculated as described previously²⁹. Briefly, the mean squared
 333 displacement, $\langle r^2 \rangle$, was calculated with overlapping time periods $\Delta t = 10 \text{ min}, 20 \text{ min}, \dots$, and
 334 plotted as a function of Δt . The first half of the plotted curve was fitted with a straight line (slope
 335 = $\langle r^2 \rangle / \Delta t$), and RMC was given by $\text{RMC} = \langle r^2 \rangle / 4\Delta t$. Module forces were recorded every 10 min and
 336 averaged throughout the simulation to yield the average traction force per module. Custom
 337 MATLAB scripts were employed to analyze the change in cell numbers in soft and stiff regions
 338 over time, to compare module forces in the soft and stiff parts of the gradients, and to track
 339 individual cells over time based on their initial location in soft or graded substrate regions.

340 On 10–100 pN nm^{-1} gradients, we found that the majority of cells translocated away from stiffer
 341 regions and toward soft areas (Fig. 3e–f), which were associated with higher traction forces per
 342 module and lower overall migration speed, RMC (Fig. 3c–d). We also tested whether altering the
 343 range of the gradient would affect the durotaxis. On 0.3–3 pN nm^{-1} gradients, the stiffer side was
 344 associated with higher traction forces and higher RMC (Fig. S9a–b). On these substrates,
 345 simulated cells displayed rapid accumulation in the stiffer regions (Fig. S9c). Finally, when the
 346 gradient was chosen such that there would be no appreciable difference in mean traction forces
 347 (100–300 pN nm^{-1}), cells clustered primarily in stiffer regions with lower RMC (Fig. S9a–b,d).

348 In order to track individual cells on stiffness gradients, and to calculate the cells' angular
 349 displacements and forward migration indices (FMI), 350 cells were simulated on a continuous
 350 200 μm gradient ranging from 10 to 30 pN nm^{-1} . Cells in a dynamic steady state were positioned

351 randomly within an approximately linear 50 μm region in the middle of the gradient (Fig. 3g) and
352 followed for an additional 14 hours of simulation time. FMIs, defined as Δy divided by the total
353 track length (accumulated distance), and where positive values denote migration toward
354 increasing stiffness, indicated that the cells moved preferentially toward the softer side of the
355 stiffness gradient – in accordance with their predicted stiffness optimum (Fig. 3h–i).

356 Supplementary Text 3: Modeling axonal pathfinding and mechanosensitive steering of
357 growth cones

358 Axonal growth cones (GCs) (Fig. S10a) can turn or contract in response to substrate stiffness
359 gradients^{24,75} by controlling the dynamics of adhesions, filopodial remodeling, and active
360 contraction³⁹. To establish whether motor-clutch dynamics could explain the mechanosensitive
361 turning of neuronal GCs²⁴, akin to the negative durotaxis exhibited by the U-251MG glioblastoma
362 cells, we modified the CMS to model an individual GC on a functionally graded substrate. A group
363 of i filopodia, each modeled as a single molecular clutch module (Fig. S10b), were attached to a
364 GC central domain. Each module was allocated n_i molecular clutches (linear springs of stiffness
365 k_c) and n_i corresponding substrate clutches (linear springs of stiffness $k_{s,i}$). Substrate clutches
366 were distributed randomly, and had values $k_{s,1} \leq k_{s,i} \leq k_{s,2}$ that varied linearly with position
367 along the gradient.

368 Monte Carlo simulations were conducted to evaluate filopodial and GC dynamics over time. We
369 modeled a GC as having 21 potential growth sites for filopodia, chosen from a uniform orientation
370 distribution between $-\pi/2$ and $\pi/2$, relative to the direction of the 'axon'. New protrusions with
371 an initial length l_{in} and width l_{wid} , dictating the effective clutch-ligand binding area, were added
372 into the simulation at a rate k_{mod} and assigned n_m myosin motors; note that we used an actin
373 filament in the schematic diagram (Fig. S11a) to represent the filament bundle in the filopodium.
374 The adhesion and substrate clutches under each filament then evolved according to the clutch
375 binding and unbinding dynamics described above. Unlike the cellular level CMS, our modified
376 model assumes a relatively stable pool of actin monomer in the GC. Thus, the actin
377 polymerization rate v_p remained constant during each simulation. See Table S3 for parameter
378 details.

379 First, we investigated whether the dozens of filopodia within a GC might enable mechanically
380 directed growth by evaluating the response of an individual 8 μm filopodium to a linear stiffness
381 gradient of 0.01 to 100 pN nm^{-1} (Fig. S10b). The filopodium was placed on a 10 μm x 10 μm square
382 substrate and oriented at an angle $0 \leq \theta \leq \pi/2$ relative to the gradient (Fig. S10c). When the
383 filopodium length was fixed, simply increasing the orientation between the filopodium and the
384 gradient was sufficient to significantly increase traction force generation (Fig. S10d). Conversely,
385 when the orientation was fixed at $\pi/2$, i.e. perpendicular to the gradient, we found that both
386 traction force and the number of engaged clutches increased linearly with filopodium length (Fig.
387 S10d).

388 Next, we investigated the impact of different stiffness gradients for traction force generation
389 using a fixed filopodium length (8 μm) and orientation (0). Maximal traction forces resulted from
390 the filopodium sensing a soft region, in the range of 0.01 to 0.1 pN nm^{-1} . The higher end of the

391 stiffness gradient proved significantly less important for the overall traction (Fig. S10e). This
392 result demonstrates that a filopodium can generate comparatively high forces even if only a part
393 of it is located on softer substrate. Thus, high traction force generation by individual filopodia is
394 favored at a low optimal stiffness and forces drastically drop on stiffer matrices.

395 Higher traction forces are often accompanied by a decrease in actin retrograde flow, as myosin-
396 borne forces are transmitted to the ECM instead of freely displacing actin. Regardless of filopodia
397 orientation, actin in GCs flows toward the structure's center, and much like traction forces, actin
398 flow rates can also differ for different types of neurons⁴⁰. We therefore investigated how both
399 the speed and direction of actin flow relative to the stiffness gradient affect the dynamics of
400 single filopodia. By studying filopodia oriented at their growing end with either the stiffer or more
401 compliant end of a stiffness gradient (Fig. S10f), we found that orientation toward the compliant
402 end of the substrate (and hence actin retrograde flow toward the stiff end of the substrate) led
403 to increased extension rates and decreased retraction rates (Fig. S10g). In all cases, the overall
404 growth rate of filopodia was a trade-off between growth at the constant actin polymerization
405 rate v_p , and shortening at the actin flow rate v_m , which varied almost linearly with substrate
406 stiffness (Fig. S10h). For an intermediate polymerization rate of $v_p = 120 \text{ nm s}^{-1}$, orientation
407 affected filopodia growth rate by a factor of two (Fig. S10h). Together, these results provide a
408 mechanism by which individual filopodia can exert more traction and elongate faster on softer
409 substrates.

410 We then investigated whether these changes in filopodial dynamics could contribute to GC
411 steering on stiffness gradients. First, we evaluated the degree of GC turning on one type of
412 stiffness gradient ($k_{s,1} = 0.01 \text{ pN nm}^{-1}$ and $k_{s,2} = 100 \text{ pN nm}^{-1}$) by studying an initially semicircular
413 GC with 21 uniformly distributed filopodia (Fig. S11a). Within 15 seconds of simulation, the
414 filopodia pointing toward the compliant end of the substrate outgrew the rest, resulting in an
415 effective turning of the GC (Fig. S11a). As expected from the previous results, filopodia in the
416 softer regions of the gradient were longer and generated higher traction forces (Fig. S11b).

417 To investigate the effect of different stiffness gradients on GC turning in detail, we repeated our
418 simulations over a broad range of possible substrate stiffnesses, with $k_{s,left}$ and $k_{s,right}$ varying
419 from 0.01 to 100 pN nm^{-1} . To quantify the degree of turning, we defined a parameter $\Lambda =$
420 $\bar{l}_{left}/\bar{l}_{right}$, which represents the degree to which the GC has turned left. Here, \bar{l}_{left} and \bar{l}_{right}
421 are the average lengths of filopodia in the left-hand and right-hand sides of the GC after 100
422 seconds of simulation, respectively. In addition to developing polarity through turning, the GC
423 could enlarge, with all filopodia elongating as compared to their initial length, or retract (Fig.
424 S11c). Enlarged GCs appeared on very compliant substrates (red section, $k_{s,left}$ and $k_{s,right}$ on
425 the order of 0.01 to 0.1 pN nm^{-1}) with a negligible stiffness gradient, and retractile GCs appeared
426 on higher stiffnesses, independent of the actual strength of the gradient (green section, $k_{s,left}$

427 and $k_{s,right}$ on the order of 1 to 100 pN nm⁻¹). Finally, polarized GCs appeared on compliant
428 substrates with a moderate or high stiffness gradient ($k_{s,left}$ on the order of 0.01 to 0.1 pN nm⁻¹,
429 ¹, >1 pN/nm/20 μm). A phase diagram for GC turning illustrates how the structure can either
430 remain straight or turn to the more compliant side (Fig. S11d), and reveals that a stronger
431 gradient may also promote GC turning, unless the range of the gradient as a whole is significantly
432 stiffer than the optimal stiffness range for individual filopodia (Fig. S11e). Thus, the motor-clutch
433 model can recapitulate mechanosensitive GC steering toward softer matrix *in silico*.

434 Table S1. Relative acrylamide and bis-acrylamide concentrations and corresponding Young's
 435 moduli for homogeneous (constant modulus) hydrogels

Final acrylamide %	Final bis-acrylamide %	Volume of (40%) AA stock, μl	Volume of (2%) bis-AA stock, μl	PBS, μl	-Young's modulus, kPa*
5.4	0.04	63	10	397	0.5
5.7	0.08	63	17.5	365	2
7.5	0.2	94	50	356	9.6
12	0.2	150	50	300	22
18	0.4	225	100	175	60

436 *Values obtained using atomic force microscopy, see Ref.³¹

437 Table S2. Parameters for the cellular level CMS

Parameter	Symbol	Value	Ref.
Total number of myosin motors	N_m	(4,000–)10,000	²⁹ , adjusted
Total number of clutches	N_c	7,500	²⁹
Maximum total actin length	A_{tot}	100 μm	²⁹
Maximum actin polymerization rate	v_p^*	200 nm/s	²⁹
Maximum module nucleation rate	k_{mod}^*	1 s^{-1}	²⁹
Module capping rate	k_{cap}	0.001 s^{-1}	²⁹
Initial module length	l_{in}	5 μm	²⁹
Minimum module length	l_{min}	0.1 μm	²⁹
Cell spring constant	k_{cell}	10,000 pN/nm	²⁹
Number of cell body clutches	$n_{c,cell}$	10	²⁹
Substrate spring constant	k_s	0.3–300 pN/nm	Adjusted
Maximum number of module motors	n_m^*	1,000	²⁹
Myosin motor stall force	F_m	2 pN	²⁹
Unloaded actin flow rate	v_m^*	120 nm/s	²⁹
Maximum number of module clutches	n_c^*	750	²⁹
Clutch on-rate	k_{on}	1 s^{-1}	²⁹
Unloaded clutch off-rate	k_{off}^*	0.1 s^{-1}	²⁹
Clutch spring constant	k_c	8 pN/nm	Adjusted
Characteristic clutch rupture force	F_b	2 pN	²⁹

438

439 Table S3. Parameters for the filopodia/GC model

Parameter	Symbol	Value	Ref.
Actin polymerization rate	v_p	90–130 nm/s	⁷⁶ , adjusted
Module nucleation rate	k_{mod}	1 s ⁻¹	²⁹
Initial filopodium length	l_{in}	3 μm	Adapted from ²⁹
Minimum filopodium length	l_{min}	0.1 μm	Adapted from ²⁹
Filopodium width for ligand binding	l_{wid}	0.2 μm	⁷⁷
Substrate spring constant (soft region)	$k_{s,1}$	10 ⁻² –10 ² pN/nm	Adjusted
Substrate spring constant (stiff region)	$k_{s,2}$	10 ⁻² –10 ² pN/nm	Adjusted
Initial number of module motors	n_m	50	²⁷
Myosin motor stall force	F_m	2 pN	²⁷
Unloaded actin flow rate	v_m^*	120 nm/s	²⁷
Initial number of module clutches	n_c	50	²⁷
Clutch on-rate	k_{on}	0.3 s ⁻¹	²⁷
Unloaded clutch off-rate	k_{off}^*	0.1 s ⁻¹	²⁷
Clutch spring constant	k_c	1 pN/nm	²⁷
Characteristic clutch rupture force	F_b	2 pN	²⁷

440 Captions for Movies S1–S3

441 Movie S1. Evolution of U-251MG glioblastoma cell distribution on photoresponsive stiffness
 442 gradient hydrogels over time. Blue overlay in the middle denotes a softer, UV-irradiated region.
 443 Vertical and horizontal lines are out-of-focus markings in the underlying glass. Scale bar, 200 μm.

444 Movie S2. Migration of individual U-251MG cells on photoresponsive stiffness gradient
 445 hydrogels. (Top) Phase-contrast data showing migrating cells over the span of 24 hours. Scale
 446 bar, 100 μm. (Bottom) Tracks corresponding to the cells in the top panel. Softer, UV-irradiated
 447 hydrogel is marked with gray color.

448 [Movie S3. DMSO- and H-1152-treated U-251MG cells migrating on stiffness gradients. Phase-](#)
 449 [contrast movies of migrating glioma cells treated with 0.1% DMSO \(left\) or 5 μM H-1152 \(right\)](#)
 450 [for 10 hours. The cells are on continuous 0.5-22 kPa stiffness gradients, in the >10 kPa region](#)
 451 [\(with substrate stiffness increasing toward the top\). Scale bar, 50 μm.](#)